ELSEVIER

Journal of Fluids and Structures 19 (2004) 449–466

JOURNAL OF FLUIDS AND STRUCTURES

www.elsevier.nl/locate/jnlabr/yjfls

Numerical simulation of vortex-induced vibration of a circular cylinder with low mass-damping in a turbulent flow

E. Guilmineau*, P. Queutey

Laboratoire de Mécanique des Fluides, CNRS-UMR 6598, Ecole Centrale de Nantes, B.P. 92101, 44321 Nantes Cedex 3, France

Received 3 July 2001; accepted 20 December 2003

Abstract

In this paper, we present some numerical results from a study of the dynamics and fluid forcing on an elastically mounted rigid cylinder with low mass-damping, constrained to oscillate transversely to a free stream. The vortex shedding around the cylinder is investigated numerically by the incompressible two-dimensional Reynolds-Averaged Navier–Stokes (RANS) equations. These equations are written in a primitive formulation in which the Cartesian velocity components and pressure share the same location at the center of the control volume. The numerical method uses a consistent physical reconstruction for the mass and momentum fluxes: the so-called consistent physical interpolation (CPI) approach in a conservative discretization using finite volumes on structured grids. The turbulence modeling is carried out by the SST K–ω model of Menter (AIAA 24th Fluid Dynamics Conference, Orlando, FL, USA). The numerical results are compared with the 1996 experimental results of Khalak and Williamson (J. Fluids Struct. 10 (1996) 455). The Reynolds number is in the range 900–15 000, the reduced velocity is including between 1.0 and 17.0. The mass ratio is 2.4 and the mass-damping is 0.013. Several initial conditions are used. According the initial condition used, the simulations predict correctly the maximum amplitude. On the other hand, the numerical results do not match the upper branch found experimentally. However, these results are encouraging, because no simulations have yet predicted such a high amplitude of vibration.

1. Introduction

Vortex shedding behind bluff bodies arises in many fields of engineering, such as heat exchanger tubes, marine cables, flexible risers in petroleum production and other marine applications, bridges, and chimneys stacks. These examples are only a few of a large number of problems where vortex-induced vibrations are important. The practical significance of vortex-induced vibrations has led to a large number of fundamental studies [see Sarpkaya (1979); Griffin and Ramberg (1982); Bearman (1984); Parkinson (1989); Blevins (1977)]. The case of an elastically mounted cylinder vibrating as a result of fluid forcing is one of the most basic and revealing cases in the general subject of vortex-induced bluff–body fluid–structure interactions. Consequently, determination of the unsteady forces on the cylinder is of central importance to the dynamics of such interactions. Despite the extensive force measurements for a cylinder undergoing transverse-forced vibration, there have appeared no direct lift-force measurements in the literature for an elastically mounted arrangement. Sarpkaya (1995) recently presented a set of drag measurements for a cylinder which can oscillate both in-line and transverse to the flow. We should also note that Hover et al. (1997) have developed a novel feedback control system to study free motions. Khalak and Williamson (1997) have presented new force measurements of lift and drag

*Corresponding author.
E-mail address: emmanuel.guilmineau@ec-nantes.fr (E. Guilmineau).

0889-9746/$ - see front matter
doi:10.1016/j.jfluidstructs.2004.02.004

for a hydroelastic cylinder of very low mass and damping. Consequently, for numerics, comparisons of forces with experimental data are difficult.

Vortex-induced vibration is generally associated with the so-called "lock-in" phenomenon where the motion of the structure is believed to dominate the shedding process, thus synchronizing the shedding frequency. Lock-in is characterized by a shifting of the vortex shedding frequency (f_s) to the system natural frequency (f_n) ($f_s \sim f_n$). Lock-in can also refer to the coalescence of the shedding, the cylinder oscillation and natural frequency ($f_s \sim f \sim f_n$). Numerous studies in vortex-induced vibration literature support the existence of lock-in [e.g., Griffin et al., (1973); Anagnostopoulos and Bearman (1992); Goswami et al., (1993); Brika and Laneville (1993); Blackburn and Henderson (1996); Fujarra et al., (1998)]. However, Gharib (1999) has noted the absence of lock-in behavior from almost all experimental studies for small mass ratios [m^* = (oscillating mass)/(displaced fluid mass)]. In almost all the literature, the problem of vortex-induced vibration of a cylinder with a large mass ratio has been well studied. However, there remain some rather basic questions concerning vibration phenomena under the conditions of very low mass and damping, for which there are few laboratory investigations. As one reduces the mass ratio to 1% of the value used in the classical study of Feng (1968), it is of significant and fundamental interest to know what is the dominant response frequency during excitation, what is the range of normalized velocity for significant oscillations or lock-in, and what is the amplitude of response as a function of normalized velocity?

Recently, Govardhan and Williamson (2000) published a review for these phenomena. Their experiments show that there exists two distinct types of response for the transverse oscillations of an elastically mounted rigid cylinder. At low mass-damping, they find three amplitude response branches, denoted "the initial branch",“ the upper branch" and "the lower branch". At high mass-damping, corresponding to the classical experiments of Feng (1968), only two branches exist; the upper branch is absent. At low mass-damping, the transitions between the modes of response are discontinuous. The mode change between initial and upper response branches involves a hysteresis. This contrasts with the intermittent switching of modes for the transition between upper–lower branches. Much recent two-dimensional numerical studies with low mass-damping or even with zero damping (Blackburn and Karniadakis 1993) and (Newman and Karniadakis 1997)) give amplitude results very similar ($A/D = 0.6$) but smaller than the expected values. For these simulations, the Reynolds number typically used is $\mathrm{Re} = 100 - 200$. In the simulations of Saltara et al. (1998) and Evangelinos (1999), the Reynolds number is higher, $\mathrm{Re} = 1000$, and the amplitude reaches values of $A/D = 0.7$. But all these simulations are carried out for low Reynolds numbers. This is contrasted with typical values of $\mathrm{Re} = 10^3 - 10^5$ for the experimental data. It seems that only the lower branch of amplitudes is picked up by the numerical simulations and the upper branch is absent. Recently, Blackburn et al. (2001) presented computations which predict the upper branch. However, these authors do not predict the amplitude of the experimental upper branch.

The main objective of this paper is to investigate numerically the dynamics and fluid forcing on an elastically mounted rigid cylinder with low mass-damping, constrained to oscillate transversely to a free stream. The numerical results are compared with the experimental data obtained by Khalak and Williamson (1996).

2. Governing equations

2.1. Fluid modeling

The aim is a computational study to predict the two-dimensional fluid motion induced by the oscillation of a circular cylinder. Equations are presented throughout in nondimensional form. The velocity scale is the reference velocity, U_∞, the length scale is the cylinder diameter, D, and time is nondimensionalized by the aerodynamic scale D/U_∞.

The unsteady incompressible Reynolds-averaged Navier–Stokes equations can be written in the following strong-conservation form, in the inertial system, i.e., the frame connected to the laboratory:

$$\nabla \cdot \boldsymbol{U} = 0, \tag{1}$$

$$\frac{\partial \boldsymbol{U}}{\partial t} + \nabla \cdot \boldsymbol{F} = \boldsymbol{0} \tag{2}$$

with the Cartesian components, F_{kj}, given by

$$F_{kj} = (U_j - \hat{U}_j)U_k + \delta_{jk}P - \frac{1}{\mathrm{Re}}\frac{\partial U_k}{\partial x_j} + \overline{u_j u_k}. \tag{3}$$

They involve the Cartesian velocity components U_k, the mesh velocity $\hat{U}_j$, the pressure P, the Reynolds stress tensor components $\overline{u_j u_k}$, the Reynolds number $\mathrm{Re} = U_\infty D/\nu$, where ν is the kinematic viscosity of fluid, and the Kronecker symbol δ_{ij}.

The resulting turbulent closure problem is solved by means of an Newtonian model as follows:

$$\overline{u_j u_k} = -\nu_t \left(\frac{\partial U_j}{\partial x_k} + \frac{\partial U_k}{\partial x_j} \right) + \frac{2}{3} K \delta_{jk}. \tag{4}$$

The eddy viscosity, ν_t, is given by the turbulence model, while the contribution of the turbulent kinetic energy K is simply neglected if the model does not use this variable. In this study, we use only the shear-stress transport (SST) $K-\omega$ model of Menter (1993). This model solves one equation for the turbulent kinetic energy K and a second equation for the specific turbulent dissipation rate ω. This model is a low-Reynolds number model. Consequently, we do not use wall functions.

For the applications to be considered, the complexity of the geometry prevents the use of Cartesian coordinates. Numerical coordinate transformations are required in order to facilitate the application of boundary conditions and transform the physical domain in which the flow is studied into a rectangular domain $\{\xi^1, \xi^2\}$. This computational domain consists of a set of unique squares of sides $\Delta\xi^i = 1, \ i = 1, 2$.

This partial transformation of Eqs. (1)–(3) yields the following equations:

$$\frac{1}{J} \frac{\partial b_j^i U_j}{\partial \xi^i} = 0, \tag{5}$$

$$\frac{\partial U_k}{\partial t} + \frac{1}{J} \frac{\partial b_j^i F_{kj}}{\partial \xi^i} = 0 \tag{6}$$

with

$$F_{kj} = (U_j - \hat{U}_j) U_k + \left(P + \frac{2}{3} K \right) \delta_{jk} - \frac{a_j^m}{\mathrm{Reff}} \frac{\partial U_k}{\partial \xi^m} - \nu_t \, a_k^n \frac{\partial U_j}{\partial \xi^n}, \tag{7}$$

where Reff is equal to $1/\mathrm{Re} + \nu_t$ and the Jacobian J of the transformation from the computational space of the coordinates $\{\xi^i\}$ to the physical space of the Cartesian coordinates $\{x_i\}$ can be expressed by $J\delta_i^j = \boldsymbol{a}_i \cdot \boldsymbol{b}_i$. The area vector $\boldsymbol{b}$ is given by $\boldsymbol{b} = \boldsymbol{a}_j \times \boldsymbol{a}_k$ (i, j, k in cyclic order) and the modulus of the covariant vector $\boldsymbol{a}_i$ by $\boldsymbol{a}_i = \partial \boldsymbol{R}/\partial \xi^i$, where, $\boldsymbol{R}$ is the position vector.

The boundary condition on the cylinder surface is the no-slip condition

$$U_i = \hat{U}_i. \tag{8}$$

The mesh moves in block and we assume that the outer boundary is far; so the fluid is not influenced by the movement. Hence, at the outer boundary, the velocity $\boldsymbol{U}$ is

$$U_1 = U_\infty, \quad U_2 = 0. \tag{9}$$

The boundary conditions for the turbulent quantities are similar to those published by Menter (1993). The following choice of free-stream value is used:

$$\omega_\infty = 1, \quad \nu_{t_\infty} = 10^{-3}, \quad K_\infty = \omega_\infty \, \nu_{t_\infty}. \tag{10}$$

Boundary conditions at no-slip surfaces are given by the following relationships:

$$K = 0 \quad \text{and} \quad \omega = 10 \left[\frac{6}{0.075 \ \mathrm{Re}(\Delta y)^2} \right], \tag{11}$$

where Δy is the distance of the first point away from the wall.

2.2. Structural dynamic modeling

Considering motion is in the transverse direction only and assuming rigid body motion, the equation of motion generally used to represent vortex-induced vibration is

$$m \, \ddot{Y} + c \, \dot{Y} + k \, Y = F_Y, \tag{12}$$

where Y is the transverse cylinder displacement, m the oscillating structural mass, c the structural damping, k the structural stiffness and F_Y the fluid force in the transverse direction.

Using the following set of nondimensional variables

$$U^* = \frac{U_\infty}{f_n D}, \qquad m^* = \frac{m}{m_d},$$
$$\zeta = \frac{c}{c_{\text{crit}}} = \frac{c}{2\sqrt{km}}, \qquad \frac{k}{m} = (2\pi f_n)^2, \tag{13}$$

where ζ the structural damping ratio, U^* the reduced velocity or the normalized velocity, m^* the ratio mass, f_n the natural frequency and m_d the displaced fluidmass ($m_d = \frac{\pi}{4}\rho D^2$), the nondimensional equation of motion for the cylinder can be written as

$$\ddot{y} + \frac{4\pi\zeta}{U^*}\dot{y} + \left(\frac{2\pi}{U^*}\right)^2 y = \frac{2}{\pi}\frac{C_L}{m^*}, \tag{14}$$

with y is the nondimensional transverse cylinder displacement and C_L the lift coefficient. We assume that the force term of the right-hand side of the equation is a constant within a time step as long as the time step is small enough. Eq. (14) is integrated in time using a fourth-order Runge–Kutta algorithm, once the force coefficient is known from the flow field calculation.

3. Numerical approach

3.1. Discrete equations

The collocated cell-centered grid lay-out is used. So, the Cartesian velocity components and the pressure share the same location at the center of the control volume (Fig. 1).

In the following, $U_k(NN)$ will be the unknown kth Cartesian velocity component at point NN and the flux at cell interface pN is identified as $(JU^i)(pN)$. The discrete divergence of the flux ϕ over the control volume is simply

$$(\Delta_i \phi^i)(NN) = \phi^1(pN) - \phi^1(mN) + \phi^2(Np) - \phi^2(Nm), \tag{15}$$

so that the discrete continuity equation results from $\phi = \boldsymbol{b}^i \cdot \boldsymbol{U}$.

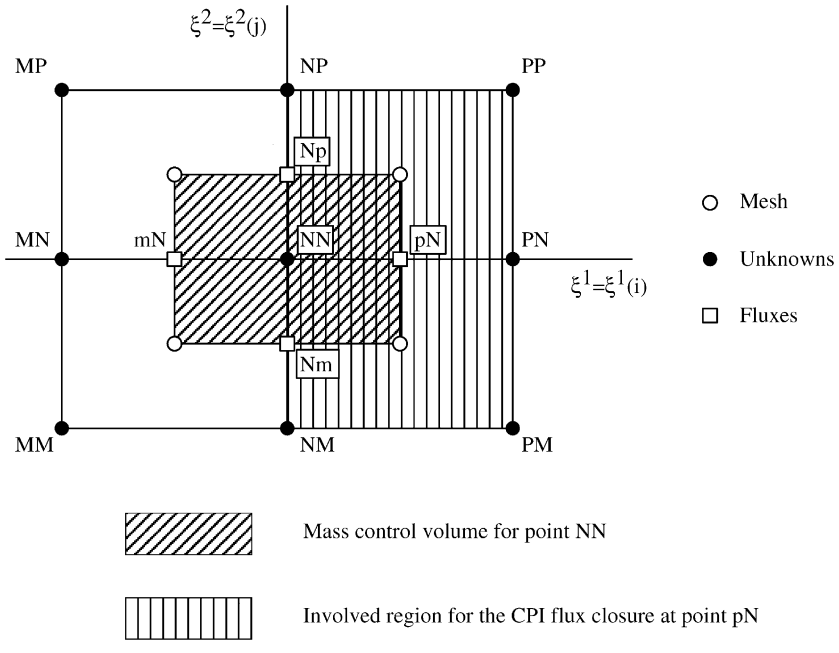

Fig. 1. Schematic sketch of presently used notation and influence stencil of point NN for CPI method.

The time derivative is discretized using a second-order accurate fully implicit backward Euler method, involving the time levels $t^0 = t - \Delta t$ and $t^{00} = t - 2\Delta t$ besides the actual time level t. We then have

$$\frac{\partial \phi}{\partial t} \approx e_1 \Phi + e_0 \Phi^0 + e_{00} \Phi^{00},$$
$$e_1 = \frac{3}{2\Delta t}, \quad e_0 = -\frac{2}{\Delta t}, \quad e_{00} = \frac{1}{2\,\Delta t},$$
$$\Phi = \phi(t), \quad \Phi^0 = \phi(t^0), \quad \Phi^{00} = \phi(t^{00}). \tag{16}$$

Eq. (15) and (16) yields the following motion equations:

$$\frac{1}{J(NN)} \Delta_i (b_j^i U_j)(NN) = 0, \tag{17}$$

$$e_1 U_k(NN) + e_0 U_k^0(NN) + e_{00} U_k^{00}(NN) + \frac{1}{J(NN)} \Delta_i (b_j^i F_{kj})(NN) = 0. \tag{18}$$

In the discrete divergence at point NN in Eq. (18), the linearized momentum flux $\boldsymbol{b}^i \boldsymbol{F}_k$ is defined at interfaces pN, mN, Np and Nm as indicated in Eq. (15). For instance, we have

$$\boldsymbol{b}^i \boldsymbol{F}_k(pN) = \left[[\boldsymbol{b}^i \cdot (\boldsymbol{U}^* - \hat{\boldsymbol{U}}) U_k + \left(P + \frac{2}{3} K \right) b_k^i - \frac{\boldsymbol{b}^i \cdot \boldsymbol{a}^m}{\mathrm{Reff}} \frac{\partial U_k}{\partial \xi^m} - \nu_t \, \boldsymbol{b}^i \cdot \boldsymbol{a}^n \frac{\partial U_j}{\partial \xi^n} \right] (pN), \tag{19}$$

where $\boldsymbol{U}^*$ is a prediction of the velocity field at the actual time. An iterative procedure is thus required at time t in order to update $\boldsymbol{U}^*$, starting with $\boldsymbol{U}^* = \boldsymbol{U}^0$.

3.2. The reconstruction problem

After integrating fluxes over the control volume, it appears that besides unknown nodal values of the Cartesian velocity components, expressions such as Eq. (19) involve the values $U_k(pN)$ which are also unknown, but at points which are not nodal points. These Cartesian velocity components are denoted by $U_k(f)$, where f is pN, mN, Np or Nm. This introduces the so-called reconstruction problem: fluxes such as $U_k(pN)$ which are not defined at nodal points must be expressed in terms of nodal unknowns. The interpolation procedure, which solves the reconstruction problem, must avoid spurious pressure modes which may exist when collocated grids are used. One of the most efficient ways to overcome this difficulty is to use a physical interpolation approach in which a velocity value such as $U_k(pN)$ is expressed not only in terms of values of U_k at the neighboring nodes of pN, the set of which (Fig. 1) is denoted $NB(pN) = \{NN, PN, PM, PP, NP, NM\}$, but also in terms of values of other velocity components and pressure at $NB(pN)$. The most classical approach in this respect is the Rhie and Chow interpolation (Rhie and Chow, 1983). Its drawbacks, as well as those of another interpolation practice due to Schneider and Raw (1987), have been analyzed by Deng et al. (1994a, b), where the so-called consistent physical interpolation (CPI) method is proposed. The application of the CPI to unsteady laminar flows has been further developed by Deng et al. (1994a) for airfoil problems and extended to turbulent flow by Guilmineau et al. (1997a).

The CPI method determines $U_k(pN)$ from the solution of the convective form of the momentum equations at point pN. This interpolation involves the set of neighbors $NB(pN)$ of influencing node (Fig. 1). For other interfaces of the control volume, the sets of active neighbors are

$$NB(mN) = \{MN, NN, MP, NP, MM, MN\},$$
$$NB(Np) = \{NN, NP, NM, PM, PN, PP\},$$
$$NB(Nm) = \{NN, PN, MN, PM, NM, MM\}.$$

Upon substitution of closures written at pN, mN, Np and Nm into the discrete momentum equation (18), where relations such as Eq. (19) have been accounted for, we obtain the discrete scheme for the momentum equations where the velocity and pressure unknowns are located only at NN and at the eight nodal neighbors of the set $NB(NN) = \{MM, MN, MP, NM, NP, PM, PN, PP\}$. The substitution of the same closures into Eq. (17) yields a discrete scheme for a nine-point pressure equation. Its ensures a second-order accuracy and numerical stability (Deng et al., 1994b). Another important feature of the CPI scheme is that it ensures both mass and momentum conservation over the same control volume.

3.3. Pressure-velocity coupling algorithm

The algorithm which yields a coupled solution of the momentum equation and the continuity equation is directly inspired by the pressure implicit with splitting of operators (PISO) algorithm (Issa, 1985)

(a) initialize the velocity field and the pressure field at $t = t^0$;
(b) new time step $t = t + \Delta t$;
(c) start iterative procedure with $U_k = U_k^0$, $P = P^0$, $U_k(f) = U_k^0(f)$, $K = K^0$, $\omega = \omega^0$;
(d) compute the turbulent quantities from filed of step (c);
(e) compute the reconstruction coefficients from the flow field of step (c) and turbulence field of step (d);
(f) solve the momentum equations to obtain a new prediction for U_k;
(g) solve the continuity equation to obtain pressure P with coefficients obtained from step (e) and U_k from step (f);
(h) correct the velocity field with coefficients from step (e), U_k from step (f) and P from step (g);
(i) reconstruction at interfaces to get $U_k(f)$ with coefficients from step (e), P from step (g) and U_k from step (h);
(j) if the nonlinear residuals are not low enough, go to step (c) and update the iteration count within the time step;
(k) solve the cylinder displacement equation;
(l) go to step (a) and update t.

4. Initial conditions

To start a computation at a normalized velocity U^* and a Reynolds number Re given, we need to initialize the flow. Thus, three initial conditions are used.

(i) Firstly, the condition denoted *from rest*. In this case, for each Reynolds number considered, the solution of vortex shedding behind a fixed cylinder is attempted. When the lift force becomes periodic, the elastically mounted cylinder is allowed to oscillate.
(ii) The second condition is called *increasing velocity* that is to say with the cylinder still oscillating, the wind speed is increased by the next step and the process is repeated. In this case, we initialize a simulation for a reduced velocity U^* and a Reynolds number Re given with the solution obtained for a velocity U^{*0} and a Reynolds number Re^{*0}, with $U^{*0} < U^*$ and $\mathrm{Re}^{*0} < \mathrm{Re}$.
(iii) The last condition is called *decreasing velocity*. We carry out the same thing as for the *increasing velocity* condition, but with $U^{*0} > U^*$ and $\mathrm{Re}^{*0} > \mathrm{Re}$. In the present study, the inception of *decreasing velocity* solution is from the upper end of the *increasing velocity* branch.

5. Spatial grid independence

In order to establish a grid-independent solution, computations have been performed for several meshes with 202×150, 252×187, 302×225, 352×262, 402×300 grids for a reduced velocity $U^* = 4.33$ and a Reynolds number $\mathrm{Re} = 3757$. The r.m.s displacement, y_{rms} and the maximum displacement, $y_{\max}$, are presented in Table 1. The difference in displacement between the coarse grid and the finest grid is 2% for the r.m.s. values and less than 3% for the maximum value. Hence, all computational results are obtained on the 202×150 grid mesh.

Table 1
Displacement for $U^* = 4.33$ and $\mathrm{Re} = 3757$ ($m^*\zeta = 1.3 \times 10^{-2}$, $m^* = 2.4$)

Mesh	y_{rms}	$y_{\max}$
202×150	0.410	0.582
252×187	0.405	0.573
302×225	0.402	0.568
352×262	0.402	0.567
402×300	0.402	0.567

Comparison of different grid resolutions.

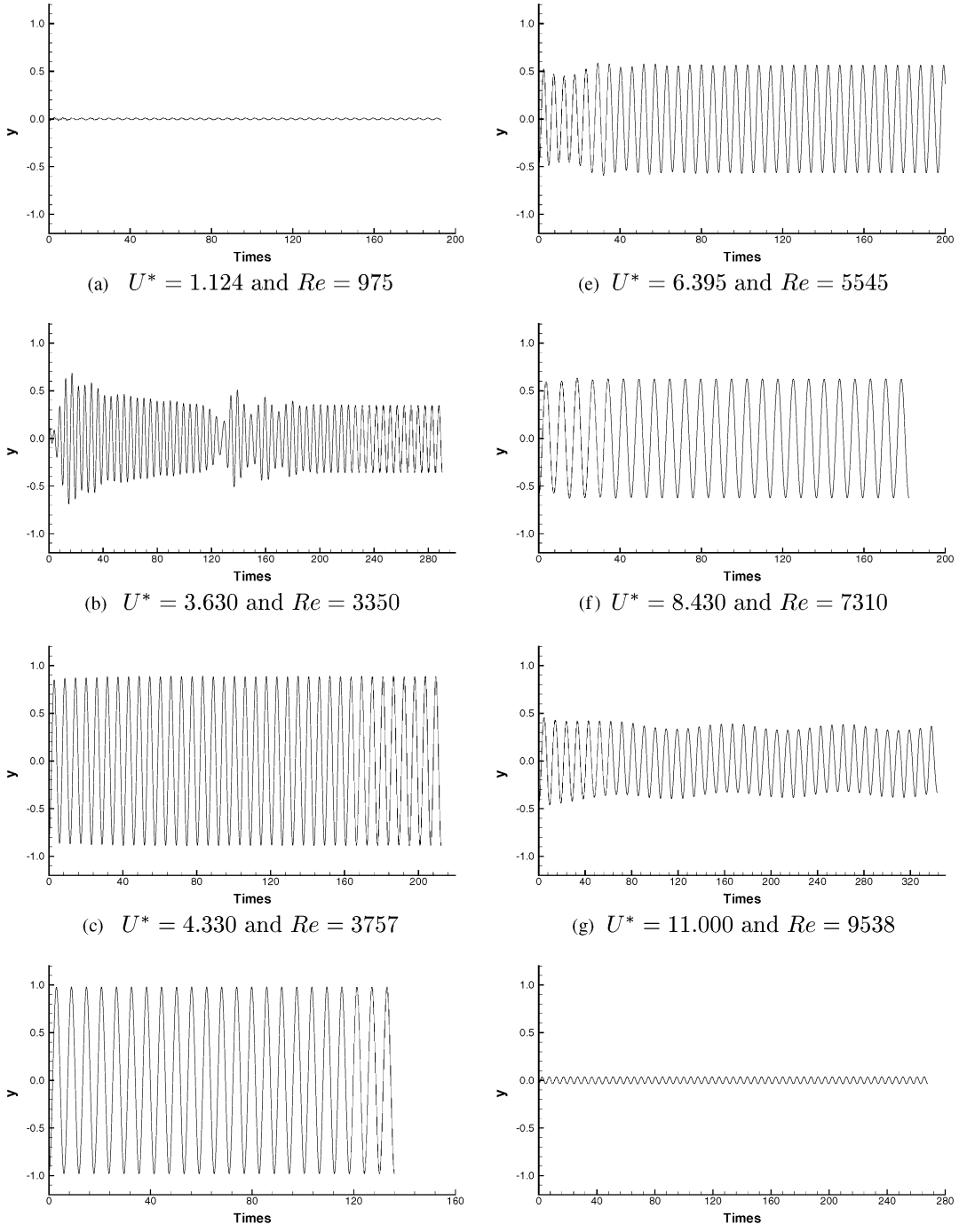

(a) $U^* = 1.124$ and $Re = 975$

(e) $U^* = 6.395$ and $Re = 5545$

(b) $U^* = 3.630$ and $Re = 3350$

(f) $U^* = 8.430$ and $Re = 7310$

(c) $U^* = 4.330$ and $Re = 3757$

(g) $U^* = 11.000$ and $Re = 9538$

(d) $U^* = 4.510$ and $Re = 3911$

(h) $U^* = 17.210$ and $Re = 14923$

Fig. 2. Cylinder displacements at different reduced velocity with the increasing velocity condition ($m^*\zeta = 1.3 \times 10^{-2}$, $m^* = 2.4$).

6. Results

6.1. Preamble

Before presenting results, some numerical parameters need to be specified. The equations are solved on an O-type structured grid. A mesh with 202 points in the angular direction and 150 points in the radial direction is used. The first points of the mesh in fluid are located at $y = 0.001D$ away from the wall what represents a maximum distance $y^+ \leqslant 0.6$ for the range of Reynolds numbers considered. The outer flow boundary is located at 25 diameter lengths away from the cylinder. A nondimensional time step, $U_\infty \Delta t/D$, equal to 0.005 is used.

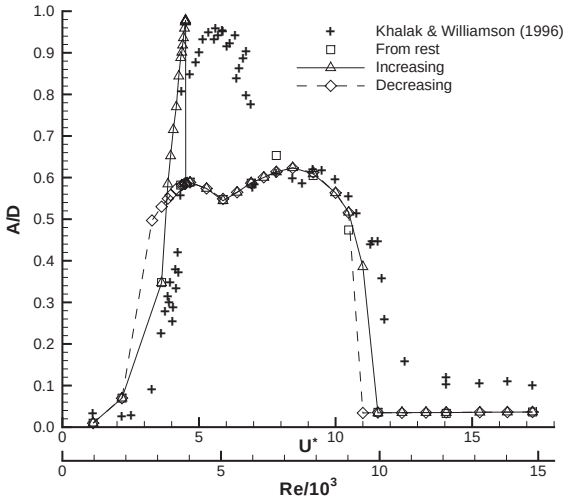

Fig. 3. Relative vibration amplitude with different initial conditions ($m^*\zeta = 1.3 \times 10^{-2},\ m^* = 2.4$).

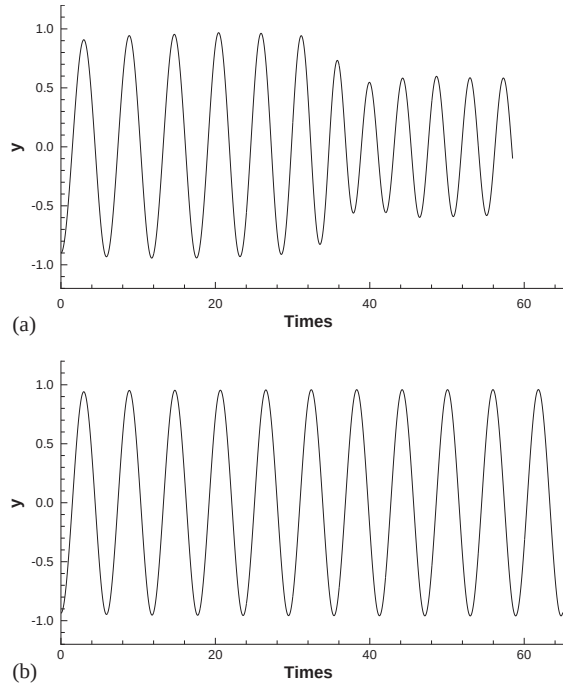

Fig. 4. Cylinder displacement for $U^* = 4.47$ and $\mathrm{Re} = 3876$ with the increasing velocity initial condition ($m^*\zeta = 1.3 \times 10^{-2},\ m^* = 2.4$): (a) $U^{*0} = 4.37$; (b) $U^{*0} = 4.43$.

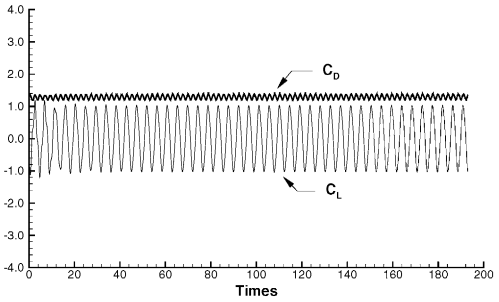

(a) $U^* = 1.124$ and $Re = 975$

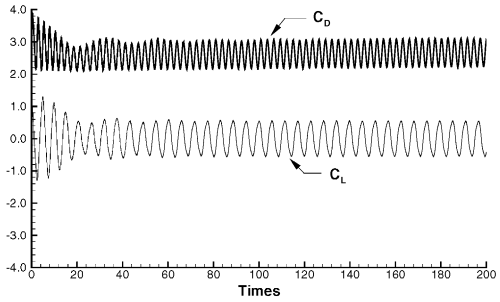

(e) $U^* = 6.395$ and $Re = 5545$

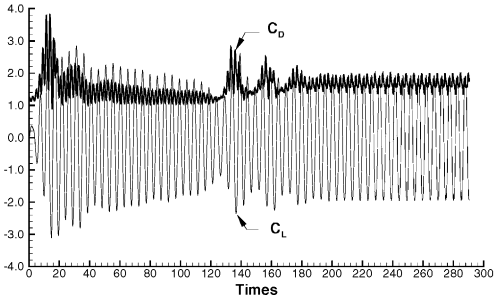

(b) $U^* = 3.630$ and $Re = 3350$

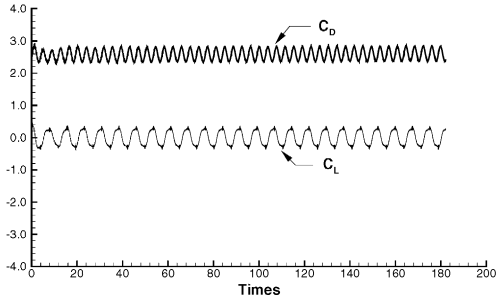

(f) $U^* = 8.430$ and $Re = 7310$

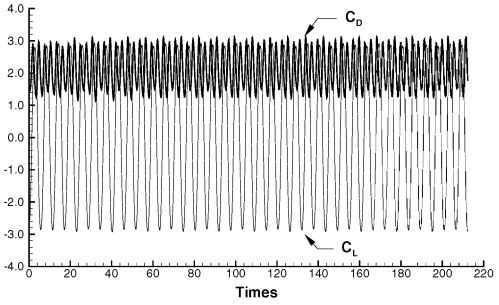

(c) $U^* = 4.330$ and $Re = 3757$

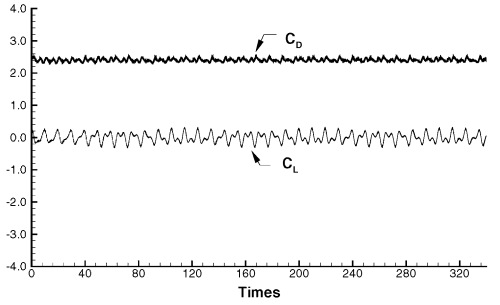

(g) $U^* = 11.000$ and $Re = 9538$

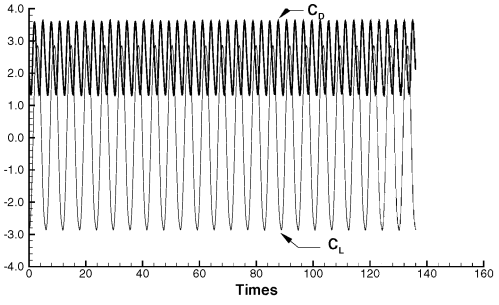

(d) $U^* = 4.510$ and $Re = 3911$

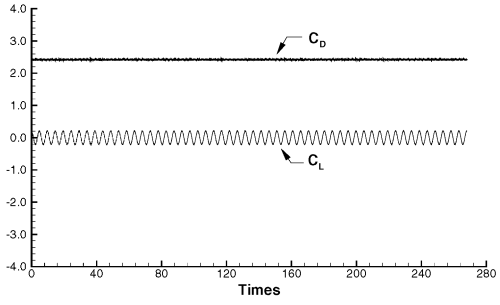

(h) $U^* = 17.210$ and $Re = 14923$

Fig. 5. Forces at different reduced velocity with the increasing velocity condition (thick line = C_D, thin line = C_L) ($m^*\zeta = 1.3 \times 10^{-2}$, $m^* = 2.4$).

For each time step, a reduction of nonlinear residuals for the discrete momentum equations is required. By default, we use a reduction by two orders of magnitude of nonlinear residuals of discrete momentum equations is carried out. Also, the divergence of the velocity field is decreased between 10^{-6} and 10^{-9}. These parameters were already used to

compute the deep dynamic stall of a pitching NACA 0012 airfoil (Guilmineau et al., 1997b) and the deep dynamic stall on several airfoil sections (Guilmineau et al., 1999).

6.2. Results

We focus on the forces and response associated with vortex-induced vibration of a rigid cylinder with low normalized mass. This problem was experimentally analyzed by Khalak and Williamson (1996). The normalized velocity U^* is included in interval 1–17. The Reynolds number ranges from 900 to 15 000. Thus, the regime is turbulent. The parameter set of the present investigation is $m^* = 2.4$, $m^*\zeta = 1.3 \times 10^{-2}$, $900 \leqslant \mathrm{Re} \leqslant 15\,000$ and $1.0 \leqslant U^* \leqslant 17.0$.

Fig. 2 presents cylinder displacements for different U^* with the *increasing velocity* condition. The simulation starts with the normalized velocity $U^* = 1.124$ (Fig. 2(a)) and the vibration amplitude of the cylinder is very small. The amplitude of vibration increases as the reduced velocity increases (Fig. 2(b) and (c)). For $U^* = 4.51$ (Fig. 2(d)), the highest oscillation amplitude occurs, the displacement of the cylinder is near to unity. After this normalized velocity, a

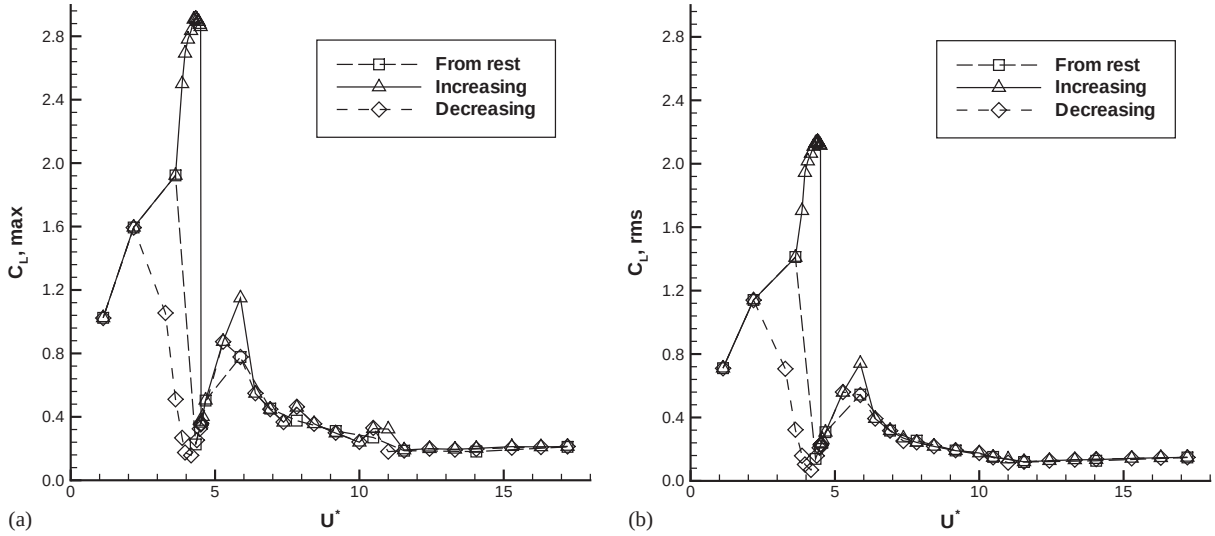

Fig. 6. Variation of lift force with different initial conditions ($m^*\zeta = 1.3 \times 10^{-2}$, $m^* = 2.4$): (a) $C_{L_{\max}}$; (b) $C_{L_{\mathrm{rms}}}$.

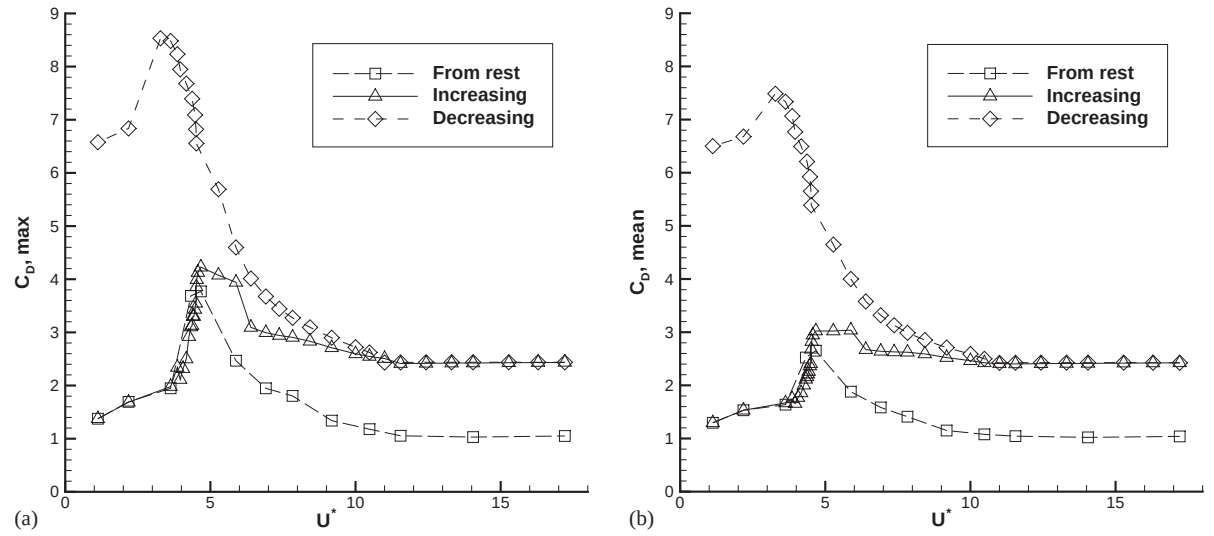

Fig. 7. Variation of drag force with different initial conditions ($m^*\zeta = 1.3 \times 10^{-2}$, $m^* = 2.4$): (a) $C_{D_{\max}}$; (b) $C_{D_{\mathrm{rms}}}$.

drop-off of the displacement amplitude occurs, and the maximum displacement of the cylinder is near to 0.6 for several values of the normalized velocity (Fig. 2(e) and (f)). Then, the vibration amplitude decreases as U^* increases (Fig. 2(g)). At the highest values of the normalized velocity, the cylinder almost does not vibrate at all (Fig. 2(h)).

The maximum amplitude for a given reduced velocity defines the response in Fig. 3. The experimental response is characterized by the initial branch, the lower branch, which are basic results, but also by a separate upper branch. For the three initial conditions, our simulations are in good agreement with experiment for the lower branch. The amplitude for the lower branch is $A/D = 0.62$, which is similar to the experimental value (Khalak and Williamson, 1996). On the other hand, numerically, we do not match the upper branch. The maximum value of the amplitude of vibration of the cylinder is obtained with the *increasing velocity* condition and $A/D = 0.98$. Experimentally, this value is $A/D = 0.96$. With the other conditions, the maximum value of the amplitude is that of the lower branch. Thus, the response amplitude depends upon the initial condition; so, this characterizes a hysteresis phenomenon. The results obtained with the three conditions are similar to the experimental results of Brika and Laneville (1993), where $m^* = 180$ and $m^*\zeta = 0.036$ for the Reynolds numbers ranging between 3400 and 11 800. However, results obtained with the *increasing velocity* condition, like in the experiment, are good because, in the literature, no simulation did predict an amplitude of vibration so high, even with moderate Reynolds numbers and low mass-damping (Khalak and Williamson, 1999).

To obtain the response given with the *increasing velocity* condition, we must use small steps of the reduced velocity. Indeed, if for $U^* = 4.47$, one uses like initial condition the flow obtained for $U^* = 4.37$, the amplitude tends towards the lower branch (Fig. 4(a)). On the other hand, if the initial condition is the flow obtained for $U^* = 4.43$, the amplitude of vibration grows slightly (Fig. 4(b)).

Fig. 5 presents forces for different reduced velocity U^* with the *increasing velocity* condition. At $U^* = 1.124$ (Fig. 5(a)), forces are extremely regular. The drag fluctuations are weaker than the lift fluctuations. At $U^* = 3.63$ (Fig. 5(b)), the transitional regime is not periodic. The drag and lift fluctuations increases as the reduced velocity increases. At $U^* = 4.51$ (Fig. 5(d)), that is to say when the cylinder reaches the maximum vibration amplitude, the force fluctuations are the more significant. After this normalized velocity, the fluctuations decrease as the reduced velocity increases. At $U^* = 11.0$ (Fig. 5(g)), forces are not periodic. At $U^* = 17.21$ (Fig. 5(h)), the drag fluctuations is almost nonexistent.

Force variations versus the reduced velocity are shown in Figs. 6 and 7 for the three initial conditions. The drag coefficient differs according to the conditions used. The drag coefficient reaches a maximum $C_{D_{\max}}$ of 8.5 with mean $\bar{C}_D$ of around 7.5 for the *decreasing velocity* condition. This is five-fold increase over the stationary case. With the *increasing velocity* condition, $C_{D_{\max}}$ is 4.22 and $\bar{C}_D$ is 3.0. The lift force $C_{L_{\max}}$ reaches 1.6, which corresponds to a maximum r.m.s. value, $C_{L_{\mathrm{rms}}}$, near to 1.1 with the *decreasing velocity* condition. With the *increasing velocity* condition, the value $C_{L_{\max}}$ is 2.9 with a r.m.s. value $C_{L_{\mathrm{rms}}}$ of 2.1. This r.m.s. value is comparable to the value of Khalak and Williamson (1997), who used the same initial condition in their experiments and $m^* = 3.3$. For low values of normalized velocity, the drag coefficient is identical with the *from rest* and *increasing velocity* conditions whereas with the *decreasing velocity* condition, it is much higher (five-fold approximatively). While for high values of U^* the drag is identical between the *increasing velocity* and *decreasing velocity* conditions, and higher than that obtained with the *from rest* condition by a

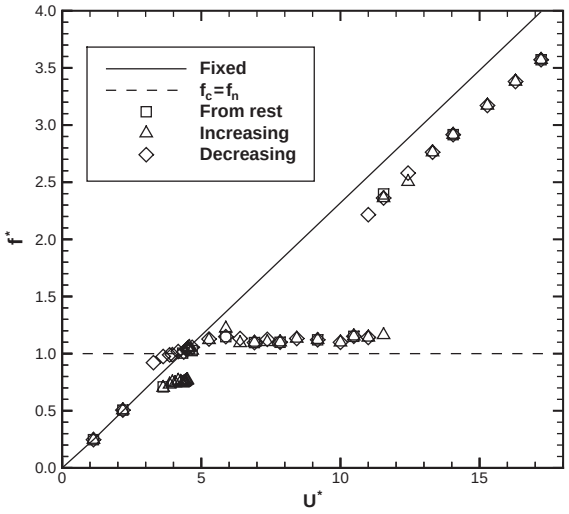

Fig. 8. Frequency response with different initial conditions ($m^* = 2.4$ and $m^*\zeta = 0.013$).

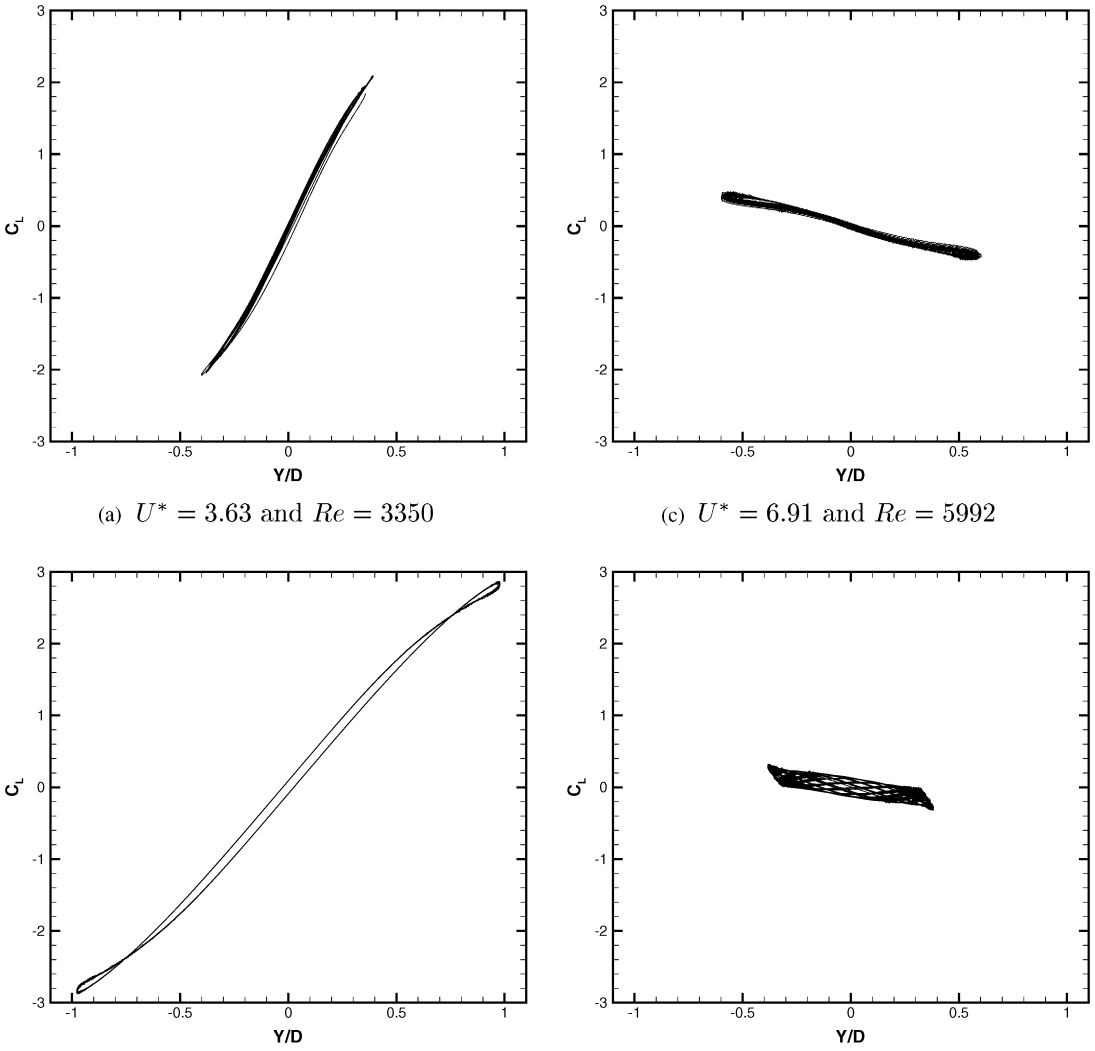

Fig. 9. Phase planes at different reduced velocity with the increasing velocity initial condition ($m^*\zeta = 1.3 \times 10^{-2}$, $m^* = 2.4$).

factor of more than two. On the other hand, the curves representing the lift coefficient are almost identical, except during the transition from the branches. These results obtained for drag are not understood.

Fig. 8 presents the frequency ratio, $f^* = f_c/f_n$ where f_c is the body oscillating frequency during induced vibration. Over the synchronization range $U^* = 4$–11, the frequency f^* is not precisely equal to unity, contrary to f^* being close to unity for large mass m^*. The frequency f^* rises to the value 1.15, which is weaker than the experimental value 1.4 (Khalak and Williamson, 1999). Similar results are being found for an elastically mounted cylinder in Khalak and Williamson (1997) and Gharib (1999). The extensive "added mass" coefficients would suggest that oscillation frequencies at large amplitude would expected to depart from unity (Khalak and Williamson, 1999).

The different branches of amplitude response are well characterized by plotting not only the amplitude but also the phase plane portraits of lift versus displacement. The Lissajou representations are presented in Fig. 9. Figs. 9(a) and (b) present the phase graphs for the initial branch. These figures indicate the periodic nature of the oscillation. Figs. 9(c) and (d) present the phase graphs for the lower branch. We can see that the graph orientation is different which implies a variation of the phase angle between lift and displacement.

The phase angle, ϕ, between the lift force and displacement is showed in Fig. 10. For all initial conditions, the shape of the curve is similar. The jump in phase is associated at the drop off of the amplitude response. Before to leave the lower branch, the phase decreases slightly for $U^* = 10.5$ and increases after this normalized velocity.

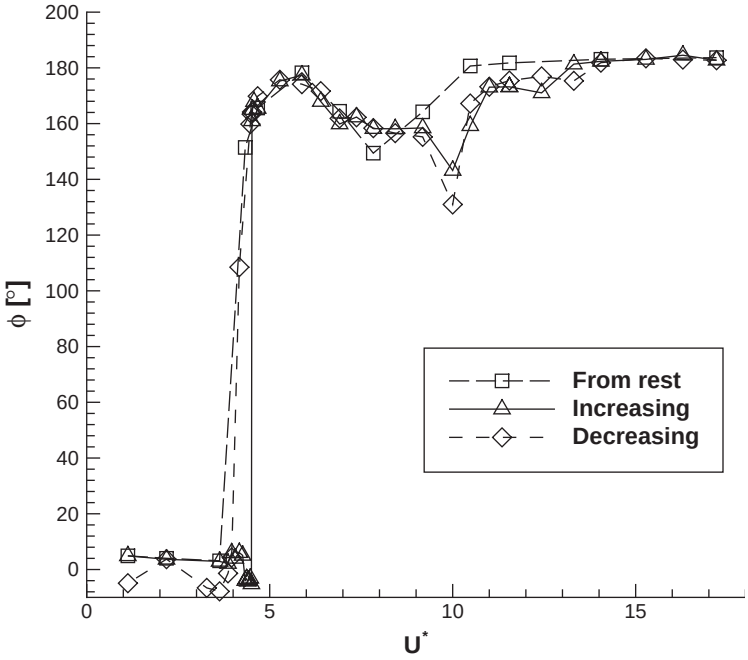

Fig. 10. Phase angle with different initial conditions ($m^* = 2.4$ and $m^*\zeta = 0.013$).

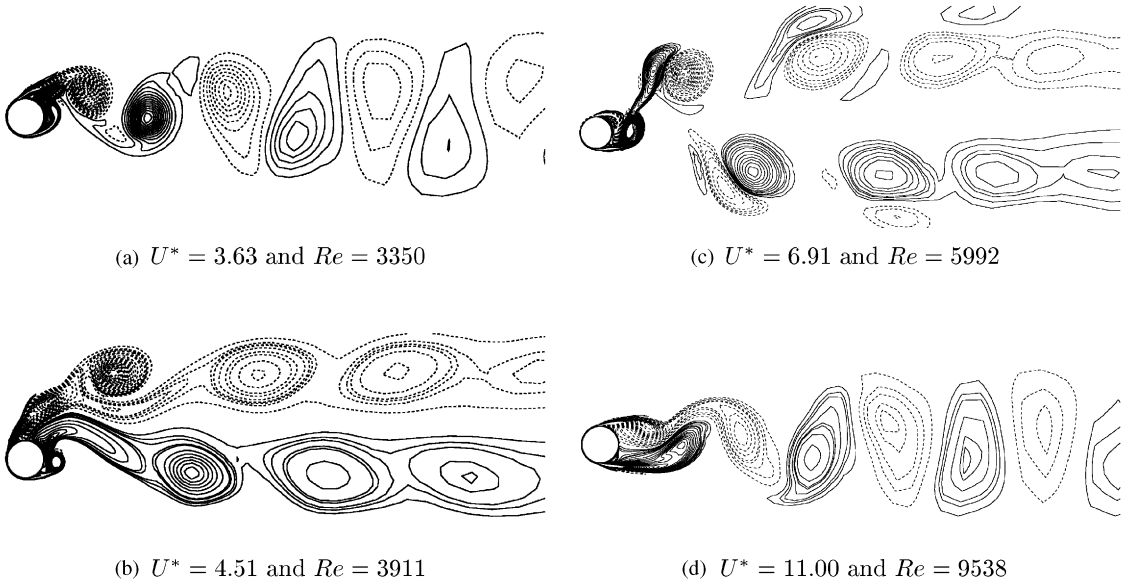

(a) $U^* = 3.63$ and $Re = 3350$

(c) $U^* = 6.91$ and $Re = 5992$

(b) $U^* = 4.51$ and $Re = 3911$

(d) $U^* = 11.00$ and $Re = 9538$

Fig. 11. Instantaneous vorticity contours for different reduced velocity with the increasing velocity initial condition ($m^* = 2.4$ and $m^*\zeta = 0.013$): ——, positive values; - - -, negative values. In all frames, the location of the cylinder is at its extreme lower position.

Fig. 11 shows the instantaneous vorticity contours when the cylinder is at the lower position. Initially, the vortex is shed from the upper surface of the cylinder (Figs. 11(a) and (b)). We can see also the 2S mode wake structure, according to the interpretation of Williamson and Roshko (1988). In the 2S mode, two vortices are generated per oscillation cycle. As U^* increases, the vortex is shed by the lower surface of the cylinder (Figs. 11(c) and (d)). A switch of vortex-shedding occurred. At the reduced velocity $U^* = 5.88$, that is to say on the lower branch, the wake structure is a 2P mode. In the 2P mode, two vortex pairs are formed per cycle. Associating the 2P mode to the lower branch have been

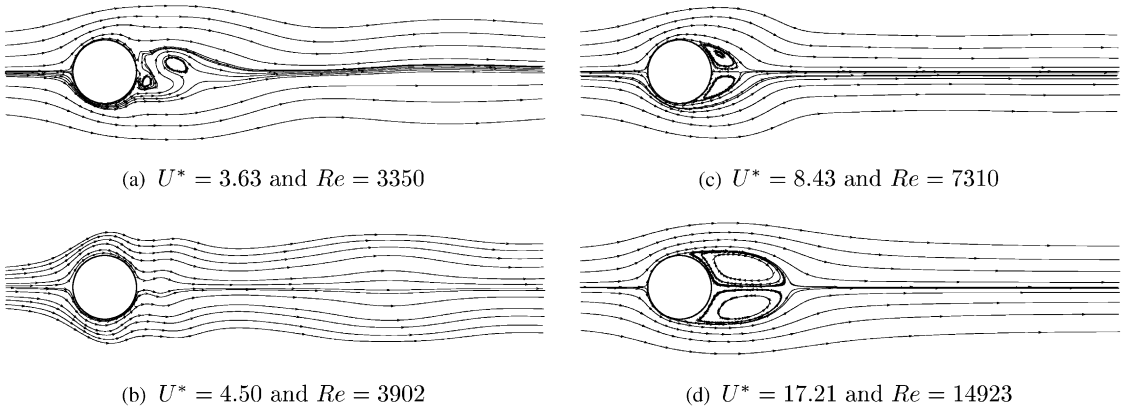

(a) $U^* = 3.63$ and $Re = 3350$ (c) $U^* = 8.43$ and $Re = 7310$

(b) $U^* = 4.50$ and $Re = 3902$ (d) $U^* = 17.21$ and $Re = 14923$

Fig. 12. Mean flow for different reduced velocity with the increasing velocity initial condition ($m^* = 2.4$ and $m^*\zeta = 0.013$).

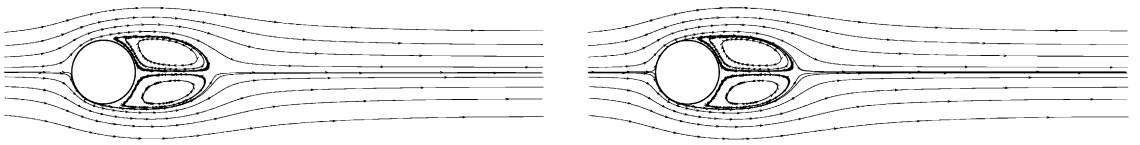

(a) From rest (b) Increasing velocity

Fig. 13. Pattern of the mean flow at $U^* = 17.21$ and Re = 14 923 with the from rest and increasing initial conditions ($m^* = 2.4$ and $m^*\zeta = 0.013$).

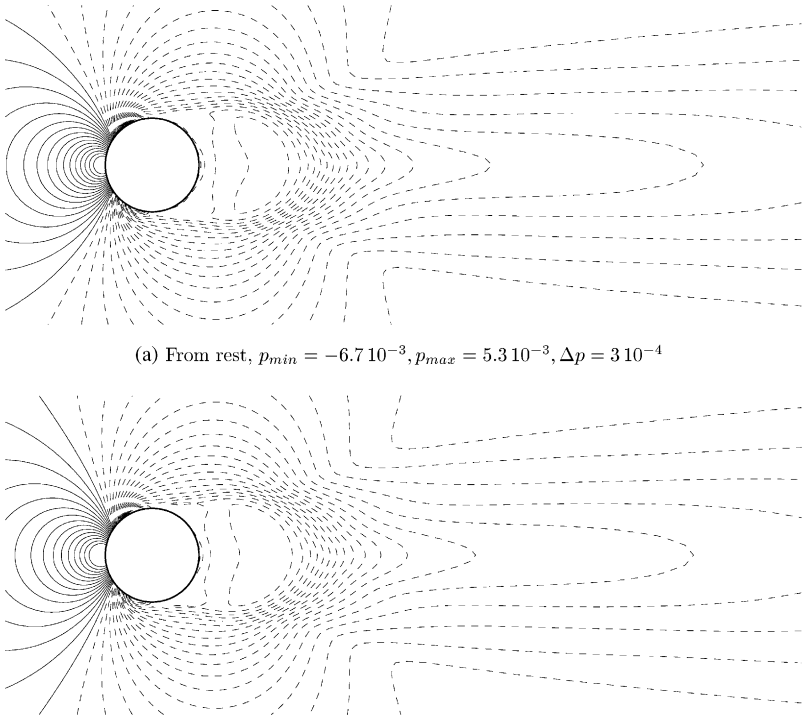

(a) From rest, $p_{min} = -6.7\,10^{-3}, p_{max} = 5.3\,10^{-3}, \Delta p = 3\,10^{-4}$

(b) Increasing velocity, $p_{min} = -3.6\,10^{-4}, p_{max} = 2.5\,10^{-5}, \Delta p = 1.7\,10^{-5}$

Fig. 14. Isopressure lines for the mean flow with the from rest and increasing velocity initial conditions at $U^* = 17.21$ and Re = 14 923 ($m^* = 2.4$ and $m^*\zeta = 0.013$): ——, positive values; - - -, negative values.

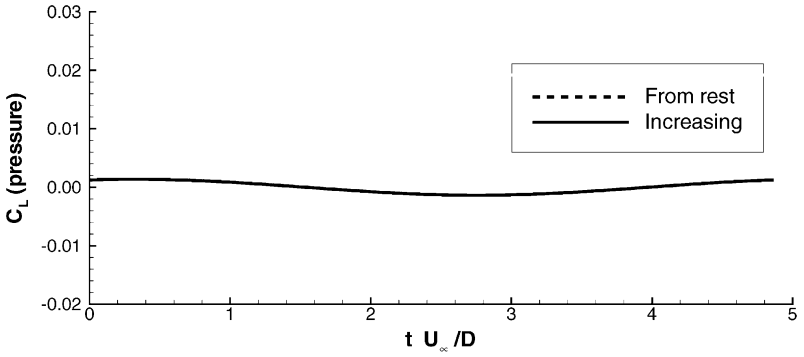

(a) Viscous

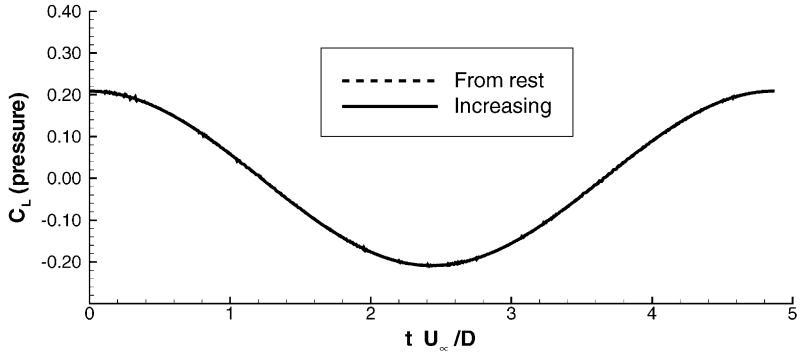

(b) Pressure

Fig. 15. Viscous and pressure lift coefficient with the from rest and increasing velocity initial conditions at $U^* = 17.21$ and Re = 14 923 ($m^* = 2.4$ and $m^*\zeta = 0.013$).

already noted by Brika and Laneville (1993). It appears that for the 2P mode, the vortices expand more laterally than for the 2S mode. At $U^* = 11.55$, after the lower branch, the pattern is similar to the flow structure at $U^* = 3.63$, but out of phase, owing to the vortex switching.

Fig. 12 presents the mean flow for different reduced velocity. In the initial branch (Fig. 12(a)), a vortex-shedding exists. At the normalized velocity $U^* = 4.50$ (Fig. 12(b)), i.e. near the reduced velocity where the cylinder oscillates the more, the flow is attached to the cylinder. And when the reduced velocity increases, the for the lower branch, the flow separates but remains attached to the cylinder. The recirculation length increases as the reduced velocity increases.

We saw that for high values of the reduced velocity, the drag differs according to the initial conditions used whereas the lift is identical. We are interested in the results obtained with *from rest* and *increasing velocity* conditions for the normalized velocity $U^* = 17.21$ and Re = 14923. Fig. 13 presents the streamlines for the mean flow. We observe that the structure of the flow is identical in both cases. However, the flow obtained with the *increasing velocity* condition is less intense than that obtained with the *from rest* condition. This is visible in Fig. 14 which presents the isopressure lines of the mean flow. One realizes that the pattern of the isopressure lines are identical in both cases, but the extrema are different. If we split the lift coefficient into a viscous part and a pressure part (see Fig. 15), for both initial conditions, we can see any difference. Now, if we split the drag coefficient into viscous part and pressure part (see Fig. 16), the viscous part is identical for both initial conditions, but the pressure part is different. The pressure drag obtained with the *increasing velocity* conditions is higher than the pressure drag obtained with the *from rest* condition.

7. Conclusions

This numerical study of vortex-induced vibrations of a circular cylinder with low mass-damping shows the steady response of the cylinder is a hysteresis phenomenon. Three initial conditions have been used: *from rest*, *increasing velocity* and *decreasing velocity*. According these initial conditions, the response of the cylinder differs. With the *from*

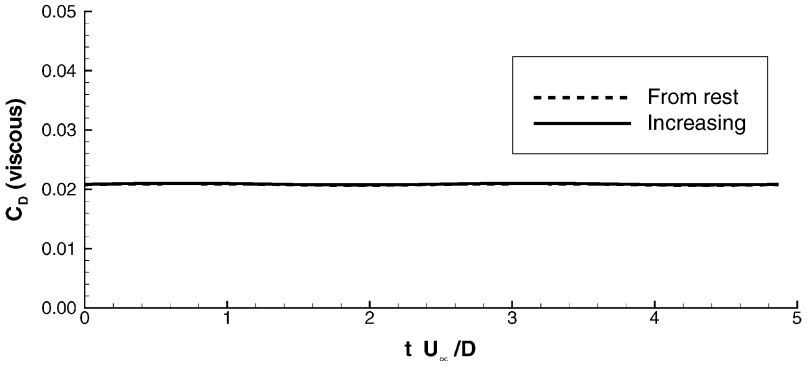

(a) Viscous

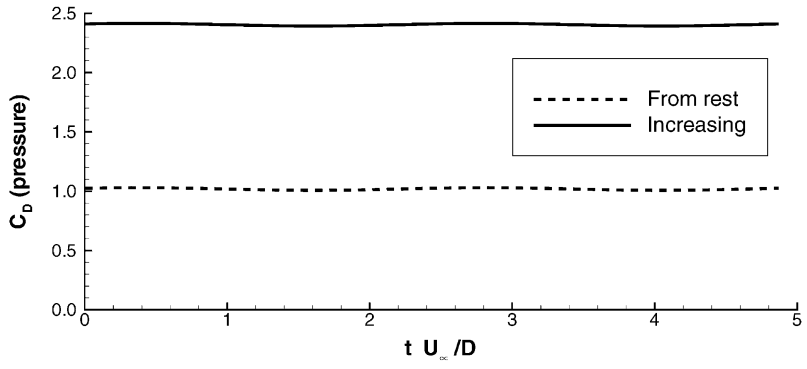

(b) Pressure

Fig. 16. Viscous and pressure drag coefficient with the from rest and increasing velocity initial conditions at $U^* = 17.21$ and Re = 14 923 ($m^* = 2.4$ and $m^*\zeta = 0.013$).

rest and *decreasing velocity* conditions, the simulations predict only the lower branch. On the other hand, with the *increasing velocity* condition, the maximum vibration amplitude corresponds to the experimental value, but the upper branch does not match experiment. To obtain this value, we had use small steps of the reduced velocity. All simulations predict correctly the amplitude of vibration on the lower branch. However, these results are encouraging, because no simulations have predicted such a high amplitude of vibration (Khalak and Williamson, 1999).

Flow visualization of the modes indicates that the initial branch is associated with the 2S mode of vortex formation, while the lower branch corresponds with the 2P mode. These remarks have been confirmed experimentally by Brika and Laneville (1993).

The response of forces on the cylinder is also an hysteresis phenomenon, particularly for the drag. In fact, the drag coefficient differs according to the initial condition used. For a low reduced velocity, drag obtained with the simulation with the *decreasing velocity* initial condition is five times as high as the one obtained with the simulation with the *from rest* or *increasing velocity* initial conditions. On the other hand, for a high-reduced velocity, the simulations give the same drag coefficient for the simulations used the *increasing velocity* or *decreasing velocity* initial conditions. This is a two-fold increase over the value obtained with the *from rest* initial condition. But, the lift coefficient is identical for all initial conditions. However, for a normalized velocity, the flow structure is identical independently of the initial conditions, but the flow is more or less intense according to the initial condition used. These results obtained for drag are not understood and these phenomena suggest validations from experimental measurements are needed.

Acknowledgements

The authors gratefully acknowledge the Scientific Committee of IDRIS (projects 00.0129 and 01.0129) for the attribution of CPU time on the Nec SX5 of IDRIS. The authors are also grateful to Charles H.K. Williamson for placing his experimental data at our disposal and for helpful discussions.

References

Anagnostopoulos, P., Bearman, P.W., 1992. Response characteristics of a vortex-excited cylinder at low Reynolds numbers. Journal of Fluids and Structures 6, 39–50.

Bearman, P.W., 1984. Vortex shedding from oscillating bluff bodies. Annual Review of Fluid Mechanics 16, 195–222.

Blackburn, H., Henderson, R., 1996. Lock-in behaviour in simulated vortex-induced vibration. Experimental Thermal and Fluid Science 12, 184–189.

Blackburn, H.M., Karniadakis, G.E., 1993. Two- and three-dimensional simulations of vortex-induced vibration of a circular cylinder. In: Proceedings of the 3rd International Offshore and Polar Engineering Conference, Vol. 3, Singapore, pp. 715–720.

Blackburn, H.M., Govardhan, R.N., Williamson, C.H.K., 2001. A complementary numerical and physical investigation of vortex-induced vibration. Journal of Fluids and Structures 15, 481–488.

Blevins, R.D., 1977. Flow-Induced Vibrations. Van Nostrand Reinhold, New York.

Brika, D., Laneville, A., 1993. Vortex-induced vibrations of a long flexible circular cylinder. Journal of Fluid Mechanics 250, 481–508.

Deng, G.B., Piquet, J., Queutey, P., Visonneau, M., 1994a. Incompressible flow calculations with a consistent physical interpolation finite-volume approach. Computers and Fluids 23, 1029–1047.

Deng, G.B., Piquet, J., Queutey, P., Visonneau, M., 1994b. A new fully-coupled solution of the Navier–Stokes equations. International Journal for Numerical Methods in Fluids 19, 605–640.

Evangelinos, C., 1999. Parallel simulations of vortex-induced vibrations in turbulent flow: linear and non-linear models. Ph.D. Thesis, Brown University, USA.

Feng, C.C., 1968. The measurements of vortex-induced effects in flow past stationary and oscillating circular and D-section cylinder. Master's Thesis, University of British Columbia, Vancouver, B.C., Canada.

Fujarra, A.C., Pesce, C.P., Parra, P.P.H., 1998. Vortex induced vibrations experiments on a flexible cylinder. In: Proceeding of the 8th International Offshore and Polar Engineering Conference, Vol. 3, Montréal, Canada, pp. 393–399.

Gharib, M.R., 1999. Vortex-induced vibration, abscence of lock-in and fluid force deduction. Ph.D. Thesis, California Institute of Technology, USA.

Goswami, I., Scanlan, R.H., Jones, N.P., 1993. Vortex-induced vibration of circular cylinders I: experimental data. Journal of Engineering Mechanics 199, 2270–2287.

Govardhan, R., Williamson, C.H.K., 2000. Mode of vortex formulation and frequency response of a freely vibrating cylinder. Journal of Fluid Mechanics 420, 85–130.

Griffin, O.M., Ramberg, S.E., 1982. Some recent studies of vortex shedding with application to marine tubulars and risers. ASME Journal of Energy Resources Technology 104, 2–13.

Griffin, O.M., Skop, R.A., Koopmann, G.H., 1973. The vortex-excited resonant vibrations of circular cylinders. Journal of Sound and Vibration 31, 235–249.

Guilmineau, E., Piquet, J., Queutey, P., 1997a. Two-dimensional turbulent viscous flow simulation past airfoils at fixed incidence. Computers and Fluids 26, 135–162.

Guilmineau, E., Piquet, J., Queutey, P., 1997b. Unsteady two-dimensional turbulent viscous flow past aerofolis. International Journal for Numerical Methods in Fluids 25, 315–366.

Guilmineau, E., Piquet, J., Queutey, P., 1999. A numerical study of dynamic stall on several airfoil sections. AIAA Journal 37, 128–130.

Hover, F.S., Miller, S.N., Triantafyllou, M., 1997. Vortex-induced vibration of marine cable: experiments using force feedback. Journal of Fluids and Structures 11, 307–326.

Issa, R.I., 1985. Solution of the implicitly discretized fluid flow equations by operator-splitting. Journal of Computational Physics 62, 40–65.

Khalak, A., Williamson, C.H.K., 1996. Dynamics of hydroelastic cylinder with very low mass and damping. Journal of Fluids and Structures 10, 455–472.

Khalak, A., Williamson, C.H.K., 1997. Fluid forces and dynamics of a hydroelastic structure with very low mass and damping. Journal of Fluids and Structures 11, 973–982.

Khalak, A., Williamson, C.H.K., 1999. Motions, forces and mode transitions in vortex-induced vibrations at low mass-damping. Journal of Fluids and Structures 13, 813–851.

Menter, F.R., 1993. Zonal two-equation k–ω turbulence models for aerodynamic flows. In: AIAA 24th Fluid Dynamics Conference, Orlando, FL, USA.

Newman, D.J., Karniadakis, G.E., 1997. A direct numerical simulation study of flow past a freely vibrating cable. Journal of Fluids Mechanics 344, 95–136.

Parkinson, G., 1989. Phenomena and modelling of flow-induced vibrations of bluff bodies. Progress in Aerospace Sciences 26, 169–224.

Rhie, C.M., Chow, W.L., 1983. A numerical study of the turbulent flow past an isolated aerofoil with trailing edge separation. AIAA Journal 17, 1525–1532.

Saltara, F., Meneghini, J.R., Siquiera, C.L.R. 1998. The simulation of vortex shedding from an oscillating circular cylinder. In: Proceedings of the 8th International Offshore and Polar Engineering Conference, Vol. 3, Montréal, Canada, pp. 356–363.

Sarpkaya, T., 1979. Vortex-induced oscillations—a selective review. Journal of Applied Mechanics 46, 241–258.

Sarpkaya, T., 1995. Hydrodynamic damping, flow-induced oscillations and biharmonic response. ASME Journal of Offshore Mechanics and Artic Engineering 117, 232–238.

Schneider, G.E., Raw, M.J., 1987. Control volume finite-element method for heat transfer and fluid flow using collocated variables. 1. Computational procedure. Numerical Heat Transfer 11, 363–390.

Williamson, C.H.K., Roshko, A., 1988. Vortex formation in the wake of an oscillating cylinder. Journal of Fluids and Structures 2, 355–381.